Nanotechnology **8** (1997) 67–75. Printed in the UK PII: S0957-4484(97)78063-2

How does a tip tap?

N A Burnham†, O P Behrend†, F Oulevey†, G Gremaud†, P-J Gallo†, D Gourdon†, E Dupas†, A J Kulik†, H M Pollock‡ and G A D Briggs§

† Département de Physique, Ecole Polytechnique Fédérale de Lausanne, 1015 Lausanne, Switzerland
‡ School of Physics and Chemistry, Lancaster University, Lancaster LA1 4YB, UK
§ Department of Materials, Oxford University, Parks Road, Oxford OX1 3PH, UK

Received 23 September 1996

Abstract. There is a demand for good theoretical understanding of the response of an atomic force microscope cantilever to the extremely nonlinear impacts received while tapping a sample. A model and numerical simulations are presented in this paper which provide a very pleasing comparison with experimental results. The dependence of the cantilever amplitude and phase upon the sample stiffness, adhesion and damping are investigated using these simulations, and it is found that 'topographic' tapping images are not independent of sample properties, nor will it be trivial to measure materials' properties from the tapping data. The simulation can be applied to other probe microscope configurations as well.

1. The demand

The intermittent-contact mode atomic force microscope (IC AFM) [1] has been developed to overcome some of the difficulties encountered in contact force microscopy, especially of organic materials. AFM, or alternatively, scanning force microscopy (SFM), provides a way of imaging surfaces with near-atomic resolution, without any constraints on the electrical conductivity. In the contact mode, adhesion between the tip and the sample leads to a certain force between them. When the tip is displaced for scanning, a lateral force is transmitted to the sample. This can lead to distortions of soft samples, and in the worst cases to irreversible damage. In the IC AFM the tip is out of contact with the sample most of the time. Excitation of the base of the cantilever leads to almost free vibrations of the cantilever, and changes in the amplitude or frequency or phase [2] of vibration due to the proximity of the sample are measured, and used in the feedback loop to control the vertical displacement of the sample. This mode of AFM has been used to image a wide range of organic materials with nanometre-scale resolution [3–5]. The IC mechanism is thought to be the origin of the 'shear force' in near-field optical microscopy [6]. Additionally, the IC mode has also been used to overcome the problems of adhesion and surface damage of materials in UHV, thus enabling Si(111)-(7×7) surfaces to be occasionally imaged with atomic resolution [7]; in this application the cantilever was vibrated with high amplitude at resonance, and the change in resonant frequency due to the surface force gradient was detected. (The intermittent-contact mode is also sometimes known as the high-amplitude resonance mode, quasi-noncontact mode or tapping mode.) Because of the increasing presence of IC AFM within the scanning probe microscopy community, the purpose of this paper is to address the question: 'On what does the response of an IC AFM depend?'

As a vibrating cantilever approaches a surface, the first effect that it will experience is a slight attractive force. A uniform force has no effect on the frequency of a harmonic oscillator, but a force gradient does. The attractive force will increase as the tip approaches the sample, and this positive force gradient will cause a decrease in the free resonant frequency of the cantilever. This effect has been modelled for small oscillation amplitudes and fairly weak force gradients relative to the spring constant [8]. The model shows how, if the cantilever is excited below the free resonance frequency in air, the amplitude goes through a peak as the cantilever approaches the surface. In liquids the free resonance is much broader, because of the additional damping, and surface sensitivity is best achieved with a driven oscillation frequency near the second overtone of the cantilever. For optimum response this model prescribes a stiff cantilever in air and a compliant cantilever in liquids. Within the range of validity of the approximations, satisfactory agreement is found with experimental measurements.

When the tip is brought closer to the sample, there is a relatively abrupt change to a strong repulsive force as the tip touches against the sample. As the name intermittent-contact mode suggests, this repulsive force acts for a short fraction of the vibration period, so that the tip strikes briefly against the sample before bouncing off and continuing its vibration under the spring restoring force plus attractive surface forces. This might be expected to lead to an increase in the resonant frequency, and also to a rather severe limit to the amplitude of vibration. Various accounts have been produced to model this numerically in air [9–13]

and in liquids [14]. These numerical models show that the behaviour is more complicated than a simple perturbation of the harmonic behaviour, and that the abrupt change of surface forces must be taken into account in any adequate description of the behaviour of an IC AFM.

It is possible to make good measurements of the response of an IC AFM both in air and in a liquid (figure 1) [15]. In air (figure 1(*a*)), three regimes are seen as the cantilever is brought towards the sample with constant vibrational excitation near the free resonant frequency. Far away from the sample, the cantilever vibrates with a constant amplitude which is determined by the damping losses in the air and elsewhere. At a certain separation ('A' in figure 1(*a*)) the tip begins to tap against the sample, limiting the amplitude. The amplitude then reduces approximately linearly with decreasing separation (suggesting that the amplitude is limited by the distance between the cantilever rest position and the sample surface). This is the second regime. As the cantilever is brought closer still to the sample ('B'), there becomes a separation at which the amplitude of the cantilever motion drops abruptly. At this point the cantilever no longer has sufficient energy to break away from the surface adhesion, and the tip becomes stuck to the sample. The residual vibration amplitude indicates the motion of the tip relative to the root of the cantilever since a beam-deflection system is used to detect the cantilever response, and it may be that the motion of the tip itself is somewhat less than the excitation amplitude at the root. In the third regime, from 'B' onwards, the amplitude stays approximately constant but the mean deflection changes by about the same amount as any further approach to the sample.

In a liquid the free vibration of the cantilever is, to a large extent, quenched. Broad resonances can still be found, but their characteristics depend on the properties of the liquid and the shape of the container. Again, three regimes can be found, but the details are different (figure 1(*b*)). In the first regime the amplitude is again almost independent of the separation, but it is considerably smaller than in air. As the cantilever is brought towards the surface, the lower limit of the deflection begins to shift (not quite linearly), but the upper limit is scarcely changed. If the motion of the tip is examined closely, it is found that the basic sinusoidal vibration is distorted (figure 1(*c*)). If these are due to the tip hitting the sample, then they may correspond to temporary pivoting about the fulcrum formed by the tip–sample contact. As the cantilever is brought closer still, a transition to the third regime is found, in which the amplitude again becomes constant and the mean deflection changes at the same rate as the cantilever is moved. However, the transition between the second and third regimes is not as abrupt as in air: there is no capture of the tip by adhesion, and there seems to be evidence of tapping even after the mean deflection starts to follow the movement of the cantilever.

It is the purpose of this paper to present a numerical model which gives a rather complete account of these experimental observations. Ideally, a complete description of the experimental phenomena would take account of:

(a) nonlinear long-range attractive forces between the tip and the sample;

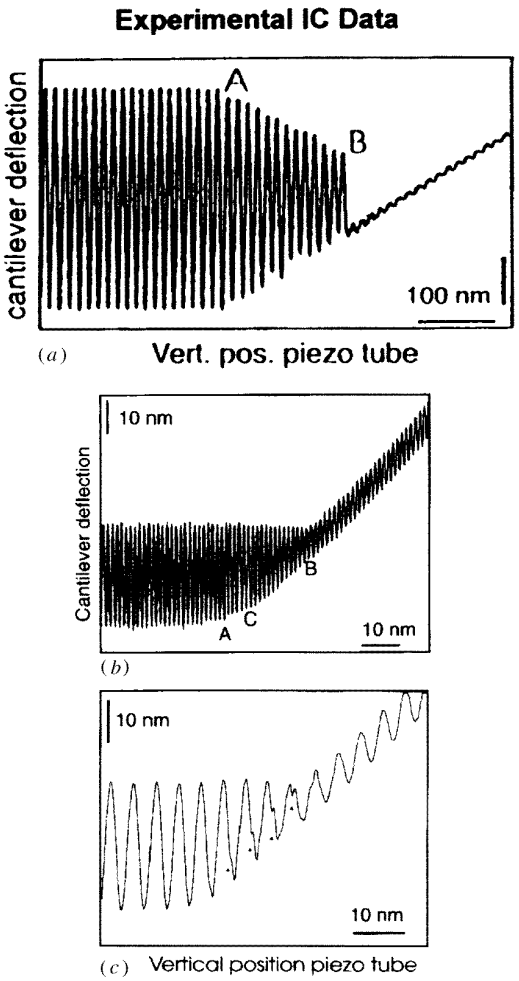

Figure 1. Oscilloscope traces (*a*) in air; (*b*) and (*c*) in water of the detected cantilever position as a function of the sample position (with permission from [15]). In (*c*) distorted features in the curves are indicated with dark triangles.

(b) the nonlinear mechanical compliance of the contact region. This in turn is affected by;

(c) the contact area itself, which is a function of the surface forces that act during contact, as well as by the externally applied load and by the elasticity and geometry of the materials.

We are not the first to numerically simulate IC AFM. As regards (a), Chen *et al* [16] assumed a Lennard-Jones attraction while Spatz *et al* [10] did not take attractive forces into account. Chen *et al* [16] treat point (c) by means of what they call a 'modified Hertz model', although $F(z)$ in their equation (4) does not take the form required by the fully modified Hertz treatment (in [17], it is known as the JKRS model); Spatz *et al*'s [10] treatment of point (b) assumes a simple linear contact stiffness, unaffected by surface forces. Of the previously published work known to us, only [9] compares theoretical with experimental results. In this paper we aim to cover all three points, as well as to give a full comparison with experimental data in order to explore the limitations of the model, and to use analytical expressions for the contact mechanics in order to minimize computing time.

The model is one which can be applied to a range of situations in which there is mechanical contact between two materials in which a vibrational excitation is applied. But because of the wide use of IC AFM, and the pressing need to be able to give a quantitative account of the contrast which is observed, we concentrate here on the application of the numerical model to the intermittent-contact mode. Specifically, we shall show that the experimentally observed behaviour in both air and liquids can be reproduced in considerable detail. We then use the model to predict the dependence of the cantilever response upon materials' properties.

2. The model

In this section we present the equations controlling the movement of the cantilever, the forces generated by the tip–sample interaction, and then the complete model. Our model does not account for plasticity of the tip or sample, but we are able to calculate the instantaneous contact pressure in order to estimate if permanent deformation occurs. Additionally, the cantilever is represented by a point mass, whereas in reality its mass is distributed. We emphasize that the tip–sample interaction used here is analytic *and* covers all possible combinations of tip and sample materials and interaction strengths *and* accounts for long-range attractive forces.

2.1. The cantilever dynamics

The starting point for the model is a driven, damped harmonic oscillator, with an additional term to describe the interaction between the sample and the tip. The motion is expressed in terms of the displacement of the tip, $d(t)$, and the position of the root of the cantilever beam $z(t)$, as depicted in figure 2. The cantilever is treated as a massless spring of stiffness k_c with a tip of effective point mass m^* at the end; the cantilever resonates at ω_c. Damping of the cantilever is introduced by a dashpot of effective damping β_c between the base of the cantilever and the tip where Q_c is the cantilever's quality factor. These effects are described by a second-order differential equation of the form

$$m^*\ddot{d}(t)+2m^*\beta_c\dot{d}(t)+k_c d(t)+P[d(t)] = k_c z(t)+2m^*\beta_c\dot{z}(t) \tag{1}$$

where $P[d(t)]$ describes the force acting on the tip resulting from the tip–sample interaction.

The complementary function of the left-hand side describes the free damped vibration of the cantilever tip, and the right-hand side is the driving term giving the particular integral. It is convenient to rearrange equation (1) to put the linear terms on the left-hand side and the term describing the nonlinear interaction between the tip and the sample on the right-hand side

$$m^*\ddot{d}(t)+2m^*\beta_c[\dot{d}(t)-\dot{z}(t)]+k_c[d(t)-z(t)] = -P[d(t)]. \tag{2}$$

The right-hand side of the equation contains the unique physics of the intermittent contact. Two separate functions are needed, one to describe the attractive force away from contact, and the other to describe the net force in contact. The choice of the appropriate contact mechanics has long been difficult and will be discussed below.

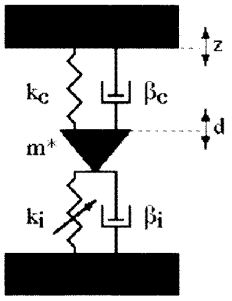

Figure 2. The coordinate system used in the model. The cantilever is assumed to behave as a simple harmonic oscillator with spring constant k_c, damping β_c, and effective mass m^*. Its tip position is d and its base position is z. The nonlinear spring k_i represents the derivative of P (equation (7)) with respect to d, and β_i is the interaction damping.

2.2. The tip–sample interaction

2.2.1. Traditional contact theories. The Poisson ratio, ν, and the Young's modulus, E, are needed to write out the reduced elastic modulus K for the tip–sample system

$$\frac{1}{K} = \frac{3}{4}\left[\left(\frac{1-\nu_{\text{tip}}^2}{E_{\text{tip}}}\right)+\left(\frac{1-\nu_{\text{sample}}^2}{E_{\text{sample}}}\right)\right].$$

It shall be convenient to use normalized variables to discuss the purely elastic contact mechanics. Similarly to the notation of [17, 18] we have for the normalized contact radius $\bar{A}$, load $\bar{P}$, penetration depth $\bar{\Delta}$ and the parameter λ:

$$\text{radius } \bar{A} = \frac{a}{\left(\frac{\pi\varpi R^2}{K}\right)^{1/3}}$$

$$\text{load } \bar{P} = \frac{P}{\pi\varpi R}$$

$$\text{depth } \bar{\Delta} = \frac{d}{\left(\frac{\pi^2\varpi^2 R}{K^2}\right)^{1/3}}$$

$$\text{parameter } \lambda = \frac{2.06}{\xi_0}\left(\frac{\varpi^2 R}{\pi K^2}\right)^{1/3} \tag{3}$$

with unnormalized variables: a the contact radius, ϖ the Dupré adhesion energy, $1/R = 1/R_{\text{tip}} + 1/R_{\text{sample}}$ the tip–sample reduced curvature, P the load, d the penetration depth and ξ_0 the equilibrium interatomic distance. In the case of an interaction potential other than Lennard-Jones, a more general definition of λ is $\lambda = 2\sigma_0(R/\pi\varpi K^2)^{1/3}$, where σ_0 is the theoretical strength of the junction. The parameter λ is very similar to the normalized neck height, μ, for a Lennard-Jones interaction introduced by Muller *et al* [19],

$$\mu = \left(\frac{2^{20}\varpi^2 R}{3^5\pi^4 K^2\xi_0^3}\right)^{1/3}$$

such that $\lambda = 0.40\mu$.

Using these normalized, dimensionless variables, the familiar Hertzian mechanics [20], which do not include attractive forces ($\varpi \to 0$), become

$$\bar{P} = \bar{A}^3 \qquad \bar{\Delta} = \bar{A}^2. \tag{4}$$

The DMT equations [21] allow surface forces but constrain the tip–sample geometry to remain Hertzian. They take the following form:

$$\bar{P} = \bar{A}^3 - 2 \qquad \bar{\Delta} = \bar{A}^2. \tag{5}$$

The JKRS theory [22, 23], subject to infinite stresses along the perimeter of the connective neck that forms between the tip and the sample, is transformed into

$$\bar{P} = \bar{A}^3 - \bar{A}\sqrt{6\bar{A}} \qquad \bar{\Delta} = \bar{A}^2 - \frac{2\sqrt{6\bar{A}}}{3}. \tag{6}$$

In the JKRS analysis there are no forces between the surfaces where they are not in contact, and infinite stresses occur at the circumference of the connective neck.

$\bar{P}$ is plotted as a function of $\bar{\Delta}$ for each of the three theories in figure 3. The applicability of each theory is determined by the assumptions on which it is based [24]. Hertzian mechanics is best for high loads or low surface forces and is therefore not appropriate for most AFM experiments. The DMT theory applies to rigid systems, low adhesion and small radii of curvature, but may underestimate the true contact area; whereas JKRS works well for high adhesion, large radii and compliant materials but may predict surface forces that are too low. A single description of all possible phenomena is provided in [19, 25], but unfortunately it requires numerical solutions. This is also the case of the comprehensive model of Greenwood [26], who has repeated the calculations of Muller *et al* [19], taking into account the Lennard-Jones force law as well as surface energy and elasticity, and giving detailed predictions for jumps into and out of contact. A set of analytical equations spanning all tip–sample parameters would be ideal.

2.2.2. A JKRS–DMT transition using a Dugdale model. Maugis [17], and Maugis and Gauthier-Manuel [18] introduces such a model in a recent publication based on the Dugdale theory [27]. In this model, by analogy with the plastic zone ahead of a crack, the adhesion is represented by a constant additive traction acting over an annular region around the contact area. The ratio of the width of the annular region to the radius of the contact area is denoted by m. The set of equations relating λ, m, $\bar{A}$, $\bar{\Delta}$ and $\bar{P}$ is

$$\begin{aligned}
1 &= \frac{\lambda\bar{A}^2}{2}\left[\sqrt{m^2-1} + (m^2-2)\arctan\sqrt{m^2-1}\right] \\
&\quad + \frac{4\lambda^2\bar{A}}{3}\left[1 - m + \sqrt{m^2-1}\arctan\sqrt{m^2-1}\right] \\
\bar{\Delta} &= \bar{A}^2 - \frac{4\lambda\bar{A}}{3}\sqrt{m^2-1} \\
\bar{P} &= \bar{A}^3 - \lambda\bar{A}^2\left[\sqrt{m^2-1} + m^2\arctan\sqrt{m^2-1}\right].
\end{aligned} \tag{7}$$

When $\bar{A} \to 0$, $m \to \infty$. Maugis shows that

$$\begin{aligned}
\bar{P}_0 &\simeq -2 \\
&\quad + \frac{8\lambda(\pi-2)}{9\pi}\left[\sqrt{4\lambda^4(\pi-2)^2 + 9\pi\lambda} - 2\lambda^2(\pi-2)\right] \\
\bar{\Delta}_0 &\simeq -\frac{8}{9\pi}\left[\sqrt{4\lambda^4(\pi-2)^2 + 9\pi\lambda} - 2\lambda^2(\pi-2)\right]
\end{aligned} \tag{8}$$

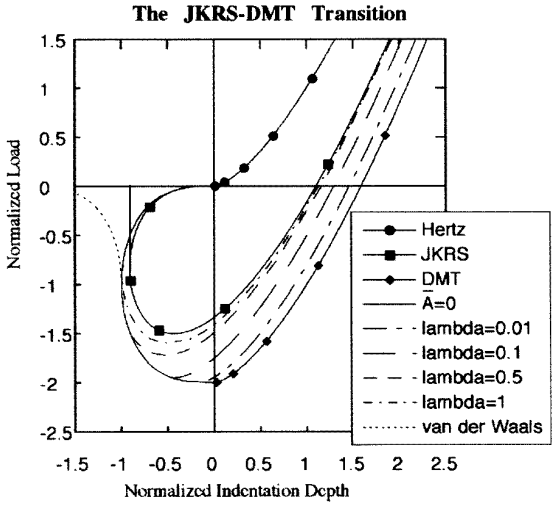

Figure 3. The traditional contact mechanical theories Hertz, DMT and JKRS, and the Maugis mechanics for various λ. Normalized load is shown as a function of normalized indentation depth or tip–sample separation. For the case of $\lambda = 1$, a van der Waals noncontact curve is also drawn. A vertical line that is the tangent to the JKRS curve ($\lambda \to \infty$) indicates the distance at which tip–sample separation occurs for stiff cantilevers.

where the subscript 0 refers to the $\bar{A} \to 0$ limit. From these latter equations, the DMT and JKRS limits can be discerned, and the importance of λ can be seen. If $\lambda \to 0$, that is, low adhesion energy and small radius of curvature with high modulus, the DMT limit is reached and $\bar{P} \to -2$ (see the DMT equation (5)). Analogously, the JKRS limit is for $\lambda \to \infty$, i.e. high adhesion and large radius of curvature for compliant systems, and $\bar{P} \to 0$, as expected from the JKRS equations (6). A continuous transition from DMT to JKRS is allowed through the use of λ. Additionally, the theory predicts that an instability always occurs when the tip–sample force is controlled (with the exception of $\lambda = 0$), and when the tip–sample displacement is controlled, the instability takes place for λ larger than about 0.94. The instability, the jump from a finite contact radius to none, generates hysteresis in quasi-static force curves even for very stiff cantilevers.

Figure 3 shows curves for various λ. Recent work from Greenwood [26] predicts similar behaviour. An earlier paper of ours [28] discussed a contact mechanical theory similar to the case when $\lambda = 0.5$.

2.2.3. Attractive forces. Away from contact the force may be taken to be an attractive one between a sphere and a surface. The van der Waals attraction between a sphere and a flat is

$$P(d) = \frac{-HR}{6(d-\xi_0)^2}. \tag{9}$$

H is the Hamaker constant, of the order of $10^{-19}J$. In the continuum limit the offset $\xi_0 = 0$; it is introduced here to prevent a singularity as $d \to 0$ and to enable the forces to be matched at the point of atomic contact [29]. Other forces, such as electrostatic, capillary or patch-charge forces [30], may readily be introduced, but they are not required to

reproduce the data of figure 1. Normalized, the expression becomes

$$\bar{P} = \frac{-\bar{P}_0(\bar{\Delta}_0 - \bar{\xi}_0)^2}{(\bar{\Delta} - \bar{\xi}_0)^2} \tag{10}$$

such that the contact and noncontact regions join at $(\bar{P}_0, \bar{\Delta}_0)$. An example is shown in figure 3 for the case when $\lambda = 1$. An approaching tip mounted on an infinitely stiff cantilever follows the van der Waals interaction to the $(\bar{P}_0, \bar{\Delta}_0)$ point before contacting the sample; whereas a receding tip follows the contact curve until $(\bar{P}_0, \bar{\Delta}_0)$ so long as $\lambda \leq 0.94$, or to the most negative value of $\bar{\Delta}$ if $\lambda > 0.94$. For example, such a tip would separate from the sample at the value of $\bar{\Delta}$ indicated by the vertical tangent in figure 3 for samples with high λ values.

2.3. The complete model

Finally we summarize the ideas put forward in this section. We commence with equation (2) which represents the cantilever dynamics and convert it into normalized form using equations (3)

$$m^*\bar{\Delta}'' + 2m^*\beta_c[\bar{\Delta}' - \bar{Z}'] + k_c[\bar{\Delta} - \bar{Z}] = -\frac{P}{\left(\frac{\pi^2\varpi^2 R}{K^2}\right)^{1/3}}. \tag{11}$$

Additionally, time may be normalized using $\tau = \omega_c t$. One may divide both sides of the above equation by k_c to obtain

$$\bar{\Delta}'' + \frac{2\beta_c}{\omega_c}[\bar{\Delta}' - \bar{Z}'] + [\bar{\Delta} - \bar{Z}] = -\frac{P}{k_c\left(\frac{\pi^2\varpi^2 R}{K^2}\right)^{1/3}}. \tag{12}$$

The final steps are to define $\bar{Q}_c^{-1} \equiv 2\beta_c/\omega_c = 2/\sqrt{2 + 4Q_c^2}$, and to realize that the normalization factor for distance is simply the normalization factors for force divided by spring constant. Then,

$$\bar{\Delta}'' + \bar{Q}_c^{-1}[\bar{\Delta}' - \bar{Z}'] + [\bar{\Delta} - \bar{Z}] = \begin{cases} -\dfrac{\bar{P}}{\bar{K}_c} - \bar{Q}_i^{-1}\bar{\Delta}' & \text{in contact} \\ \dfrac{\bar{P}_0(\bar{\Delta}_0 - \bar{\xi}_0)^2}{\bar{K}_c(\bar{\Delta} - \bar{\xi}_0)^2} & \text{out of contact.} \end{cases} \tag{13}$$

where we have added $\bar{Q}_i^{-1}\bar{\Delta}'$, defined for mathematical convenience as $2\beta_i\bar{\Delta}'/\omega_c$, to account for interaction damping. Additionally, $\bar{K}_c = k_c/(\pi\varpi R^2K^2)^{1/3}$.

$\bar{P}$ represents equations (7) which is the chosen contact mechanics for the situation where the tip and the sample are touching, and equation (10) describes the tip–sample interaction when there is no contact. This particular choice of equations satisfies points (a)–(c) in section 1 of this paper. We shall present our results in both unnormalized and normalized form.

Initial tests of the program, with completely satisfying results, were made using no cantilever oscillation in order to simulate force curve acquisitions. The program consists of a HP Veetest user interface, with calls to a Fortran program and NAG Fortran library routines. Run on a HP700, the calculations last from several seconds to several minutes. A simplified version may be run interactively with a WWW browser at http://igahpse.epfl.ch.

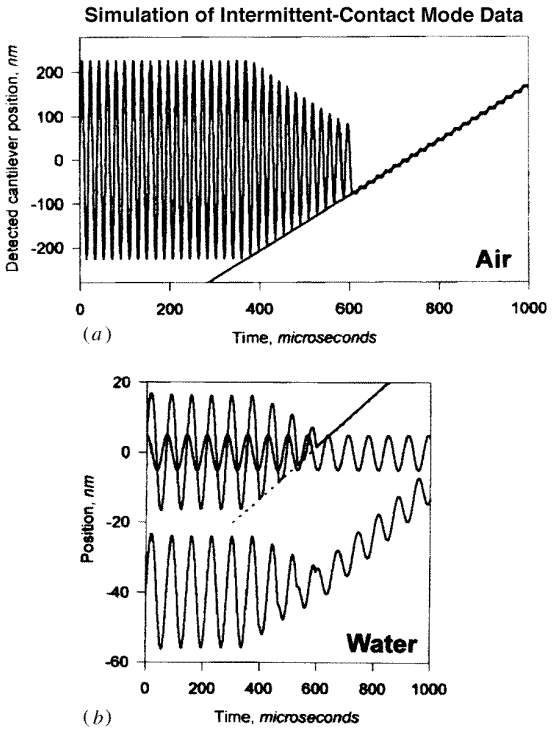

Figure 4. Simulated IC data for the experimental results of figure 1. Position (nm) is plotted as a function of time (μs). In air (*a*), where the detected cantilever and sample surface positions are shown, only negligible differences between theory and experiment can be ascertained. The values used were: $\omega_c = 2\pi \times 52$ kHz, $k_c = 0.58$ N m^{-1}, $Q_c = 40$, $K = 100$ GPa, $R = 100$ nm, $Q_i = 0.2$. In water (*b*), where the upper curves are the positions of the sample (dotted line), cantilever base (solid-fully sinusoidal), and cantilever tip (solid-partially sinusoidal), and the lower curve the detected cantilever position (i.e. the tip signal minus the base signal), the fit is not as good as in (*a*). Possible reasons for this discrepancy are discussed in the text. For water the variables chosen were $\omega_c = 2\pi \times 14.1$ kHz, $k_c = 0.38$ N m^{-1}, $Q_c = 3$, $R = 20$ nm, $\varpi = 0$ mJ m^{-2}, $K = 100$ GPa and $Q_i = 0.03$.

3. The results

3.1. Comparisons with experiments

Figure 4(*a*) shows our comparison with the experimental data of figure 1(*a*). The detected cantilever position is plotted as a function of time. The frequency, spring constant, damping and free oscillation amplitude of the cantilever were those given by the authors ($\omega_c = 2\pi \times 52$ kHz, $k_c = 0.58$ N m^{-1}, $Q_c = 40$) [15]. An elastic modulus of 70 GPa for their glass sample was used so that K was estimated to be 100 GPa and the tip radius was assumed to be 100 nm. The sharp transition from a finite cantilever amplitude to almost zero amplitude occurs with a work of adhesion $\varpi = 100$ mJ m^{-2}. The interaction damping, Q_i, was 0.2. When overlaid, only negligible differences between simulation and experiment can be discerned. The choice of the unknown parameters R, K, and Q_i used to fit the data is by no means unique.

There are four curves shown in figure 4(*b*). The top curves represent the positions in time of the cantilever

base, the cantilever tip, and the sample surface; the lower curve shows the difference between the tip and base, offset by -40 nm. The values used to generate them were: $\omega_c = 2\pi \times 14.1$ kHz, $k_c = 0.38$ N m^{-1}, $Q_c = 3$ as given by the authors or measured from their data. The following values were assumed: $R = 20$ nm, $\varpi = 0$ mJ m^{-2}, elastic modulus of glass 70 GPa and Q_i equal to 0.03. In most commercially available AFMs, it is the difference between the tip position and cantilever base position which is in fact measured, such that it is this lower curve which is the match to the experimental data of figure 1(c). When the cantilever is free and driven at its resonant frequency, there exists a $\sim \pi/2$ phase lag between the cantilever tip and base. After firm contact with the sample the measured response is out of phase with the cantilever base. The deviations from sinusoidal behaviour in the measured response originate from the shocks that the tip receives during intermittent contact with the sample. The result is the phase change from $\sim \pi/2$ to $\sim \pi$.

Although the general behaviour of figure 4(b) correlates well with figure 1(c), a close inspection reveals that the portion of the curve representing contact with the sample is offset upwards in the experimental data as compared with the simulated data and that the upper limit of the envelope of the cantilever motion decreases instead of remaining constant. This may be due to the limitations of the point-mass model that we have assumed here, that is, no higher flexural modes are accounted for. Because beam deflection detection systems record the angle of the end of the cantilever, the shape of a cantilever overtone gives an apparent cantilever amplitude greater than that of the fundamental. But after contact is established, the cantilever behaviour is identical to when driving the cantilever at its resonance. To determine if the discrepancy between the model and the experiment is because of the point-mass approximation or because of hydrodynamic effects [31] it would be useful to compare data at an overtone in both air and in water.

Experimentally, IC in liquids is carried out by exciting the sample at an overtone frequency of the cantilever [31]. We also simulated driving the cantilever by means of a spring and dashpot representing the hydrodynamic coupling between the sample and cantilever, and found results almost identical to those of figure 4(b). (The choice of values for the spring and dashpot was entirely empirical.)

3.2. Further simulations: sample properties

The simulations in figure 4 compare quite well with those of figure 1, lending credence to our approach. Now that we have some confidence in the method, what can be learned from the simulations? What affects do sample damping, adhesion, and elasticity have on the phase and amplitude of the IC signal? Figure 5 displays the results for the case when the value of ϖ was changed from 2 mJ m^{-2} to 37 mJ m^{-2} to 72 mJ m^{-2} for the values (as in figure 4(a)) $\omega_c = 2\pi \times 52$ kHz, $k_c = 0.58$ N m^{-1}, $Q_c = 40$, $K = 100$ GPa, $R = 100$ nm, $Q_i = 0.2$. As the tip–sample distance decreases, the differences between the curves increase. We have also observed, for other

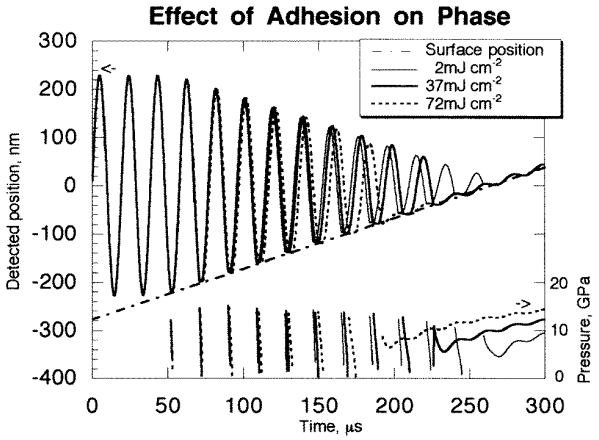

Figure 5. A simulation demonstrating how different values of the tip–sample adhesion change the cantilever's phase. Detected cantilever and sample positions (left-hand scale) and the instantaneous Hertzian pressure $Ka/\pi R$ (right-hand scale) displayed as a function of time for successive adhesion values of ϖ = 2, 37 and 72 mJ m^{-2}. The other parameters were $\omega_c = 2\pi \times 52$ kHz, k_c = 0.58 N m^{-1}, Q_c = 40, K = 100 GPa, R = 100 nm, Q_i = 0.2. The phase is changed least for the greater tip–sample distances.

values of the variables, that the differences between the curves first increase, then decrease somewhat, then increase again. A similarly complex behaviour occurs for all tip–sample properties—damping, adhesion and elasticity—so at smaller tip–sample separations the influence of the sample properties on the cantilever response is indeed strong and intricate. Note, however, that when the tapping amplitude is still a significant fraction of the free cantilever amplitude, the curves appear the same. Therefore at high setpoint amplitudes during image acquisition, it may be possible to obtain IC data independent of the properties of the sample.

Also plotted in the lower part of figure 5 is the instantaneous Hertzian pressure $Ka/\pi R$, with the appropriate scale on the right-hand side. Perhaps surprisingly, the pressure stays roughly constant as a function of tip–sample distance. For other choices of parameters that we have investigated, the pressure rises slowly with diminishing tip–sample distance before reaching the plateau. The relative phase of the three simulation runs may also be easily observed in the pressure data. Here, with large interaction damping, the pressure progressively becomes smaller during the time that the tip is in contact with the sample. For low-damping materials the pressure first intensifies before falling off.

To investigate better the role of materials properties in IC data, we calculated the detected cantilever response and instantaneous contact radius $\bar{A}$ as a function of one of the normalized variables of equation (13). More specifically, the chosen normalized variable was changed to become a function of time. All of the figures and calculations presented below were performed for the conditions of free cantilever peak-to-peak amplitude of 20 nm at ω_c, sample offset of 9 nm, $\xi_0 = 0.265$ nm, and $\bar{Q}_c^{-1} = 0.1$. The detected positions of the cantilever tip, the cantilever base, the sample surface, (left-hand scale) and the instantaneous

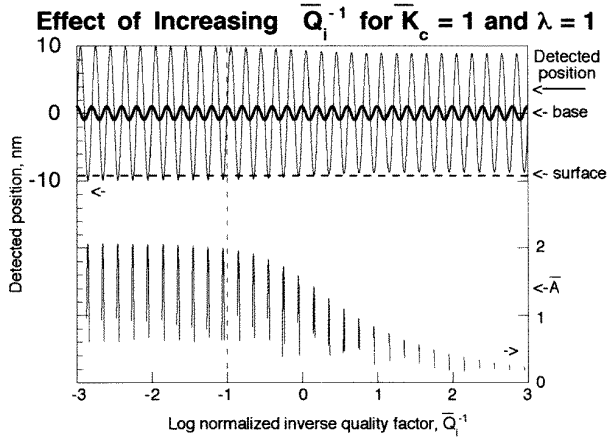

Figure 6. The value of the inverse quality factor for the tip–sample interaction, $\bar{Q}_i^{-1}$ (x-axis), was increased with time to observe the effect on the cantilever signal (left-hand scale) and instantaneous contact radius $\bar{A}$ (right-hand scale), which is directly proportional to the Hertzian pressure. Also displayed are the positions of the cantilever base (thick line) and the sample surface (thick dashed line, both left-hand scale). A 90% setpoint amplitude was chosen. The vertical dashed line refers to the value of $\bar{Q}_i^{-1}$ used in figures 7 and 8. High-damping materials greatly affect the cantilever response.

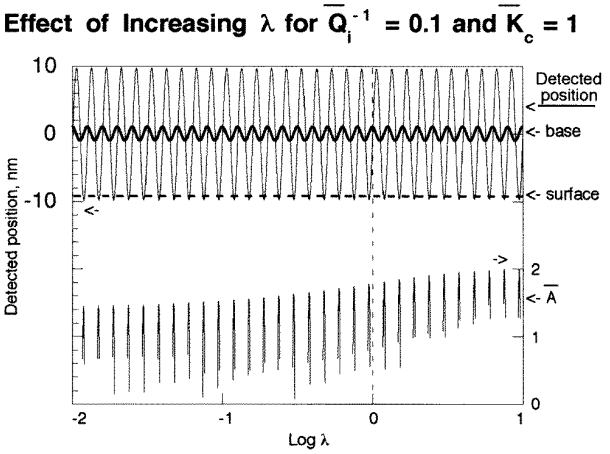

Figure 7. Here, λ (x-axis), which represents the ratio between surface energy and elastic modulus for a given tip–sample combination, was increased with time to observe the effect on the cantilever signal (left-hand scale) and instantaneous contact radius $\bar{A}$ (right-hand scale), which is directly proportional to the Hertzian pressure. Also displayed are the position of the cantilever base (thick line) and the sample surface (thick dashed line, both left-hand scale). A 90% setpoint amplitude was chosen, and at this amplitude the materials' properties (λ) do not greatly influence the cantilever amplitude or phase. The vertical dashed line refers to the value of λ used in figures 6 and 8.

contact radius $\bar{A}$ (right-hand scale) are shown in figures 6–8. Dashed vertical lines indicate the value of the x-axis variable that was used in one of the other figures. The normalized contact radius $\bar{A}$ is directly proportional to the Hertzian pressure

$$Ka^3/R\pi a^2 = Ka/\pi R = \bar{A}\left(\frac{\varpi K^2}{\pi^2 R}\right)^{1/3}.$$

3.2.1. The role of damping. In figure 6 the x-axis variable is the normalized inverse quality factor $\bar{Q}_i^{-1}$ of the tip–sample interaction, calculated for constant $\bar{K}_c = 1$ and $\lambda = 1$. The amplitude and phase of the cantilever response change for log $\bar{Q}_i^{-1}$ values greater than about -1. For higher values, energy losses are more pronounced and as a consequence the cantilever barely penetrates the surface. In fact, above log $\bar{Q}_i^{-1} = 0$, it seems as if the cantilever does not even touch the surface. Remember, however, that not only can the surface bulge out towards the tip, but the data are plotted as the *detected* cantilever position, i.e. the tip position minus the cantilever base position. This behaviour remains the same for other combinations of $\bar{K}_c$ and λ.

Note that for log $\bar{Q}_i^{-1} \leq 0$ the shape of $\bar{A}$ during each strike of the surface is roughly symmetrical and contact is made and broken at nonzero values of $\bar{A}$. The cantilever has enough kinetic energy to pass over the attractive potential. For $1 \leq \log \bar{Q}_i^{-1} \leq 3$ where the cantilever loses a lot of energy because of the high damping, there exists hysteresis in the contact radius $\bar{A}$, that is, contact is formed at a higher $\bar{A}$ than when contact is lost, as during quasi-static force curve acquisition.

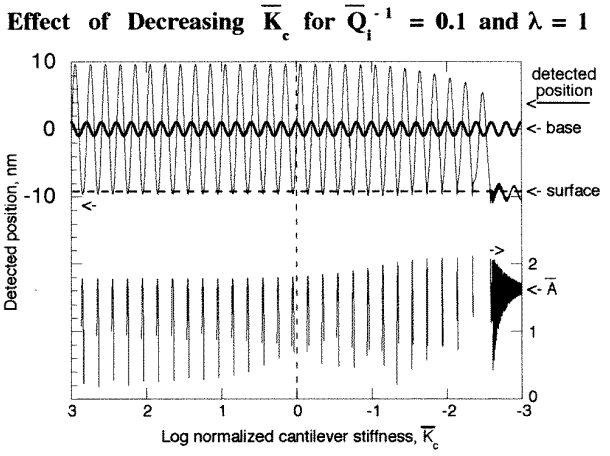

Figure 8. The normalized cantilever stiffness $\bar{K}_c$ (x-axis) was increased with time to observe the effect on the cantilever signal (left-hand scale) and instantaneous contact radius $\bar{A}$ (right-hand scale), which is directly proportional to the Hertzian pressure. The position of the cantilever base (thick line) and the sample surface (thick dashed line, both left-hand scale) are also displayed. A 90% setpoint amplitude was chosen. The vertical dashed line indicates the value of $\bar{K}_c$ used in figures 6 and 7. Not until the cantilever becomes very weak does its behaviour alter.

3.2.2. The role of λ. The influence of λ for the case of $\bar{Q}_i^{-1} = 0.1$ and $\bar{K}_c = 1$ is displayed in figure 7. The amplitude and phase of the cantilever stay remarkably constant, although the increase in the maximum $\bar{A}$ for each cycle does mean that the cantilever progressively indents the sample surface with increasing λ. This constancy was observed for almost all values of $\bar{K}_c$. Only with $\bar{K}_c < 0.05$,

such that the cantilever was about to become trapped by the sample, was there significant variation in its response. Indeed, above the $\bar{\Delta}$-axis, the normalized Maugis curves in figure 3 are very similar, so that for a tip with enough kinetic energy to pass over the attractive potential, there should not be a strong dependence on λ.

3.2.3. The role of cantilever stiffness. The normalized cantilever stiffness, $\bar{K}_c$, is the independent variable in figure 8, where $\bar{Q}_i^{-1} = 0.1$ and $\lambda = 1$. The effective mass of the cantilever was decreased so as to maintain a constant resonant frequency. Thus, the energy of the cantilever decreases until the cantilever is trapped by the interaction. The phase and amplitude do not change significantly until $\bar{K}_c < 0.1$. Then its amplitude and contact time decrease and its phase becomes retarded, although the minimum and maximum contact radii stay roughly constant. When the tip is captured by the surface, ringing is observed.

3.2.4. Effect of sample properties on metrology, topography and phase-contrast imaging. These preliminary calculations indicate that if the cantilever energy is high, the tip–sample distance large, and the interaction damping low, then the cantilever response is to first order and independent of sample properties. Thus, there is some hope that for low-damping materials (metals, etc), topographic images acquired using the IC amplitude as a setpoint can be used for metrological purposes. Under the same conditions for high-damping materials (polymers, etc) the cantilever response is most sensitive to the damping, as opposed to adhesion or elastic modulus. As of yet, we have not observed conditions under which the phase changes, but the amplitude does not. Therefore interpretation of phase-contrast imaging [2] eludes us.

We must caution that our model does not account for plasticity of materials, which could act as a source of energy dissipation. In order for the predictions above to hold, the elastic limit of the system must not be exceeded. The instantaneous contact pressures easily reach into the GPa range, as is the case in figure 5.

3.3. The significance

The model which we have presented here works well for IC AFM. It is able to give a good account of experimental data, in particular of measurements of the behaviour of a vibrating cantilever as it approaches and comes into contact with a surface, both in air and in a liquid. It predicts changes in vibration amplitude, and also the occurrence of distorted features in the vibration when intermittent contact occurs with the sample. This gives confidence in the application of the model to simulations of images in IC AFM. It also suggests that the model will be applicable to image simulations for other situations, such as frequency modulation due to gradients in the attractive surface forces, by which atomic resolution AFM imaging in UHV can be achieved [7]. This is a simpler situation, because the severe nonlinearities associated with the cyclical transition between noncontact and contact are not present. This transition is the most difficult part of the model to get correct, and the fact that it works so well here may mean that this aspect can also be applied to configurations where the mode of excitation is different. It may, for example, provide a useful model for ultrasonic force microscopy [32, 33] or scanning local-acceleration microscopy [34], in which the excitation is provided by elastic waves from a transducer placed underneath the sample. The observation of nanosubharmonics and chaos in such a configuration at high ultrasonic amplitudes undoubtedly depends on the nonlinear properties of the tip–sample interaction [35].

These illustrative calculations support what is already empirically known about the conditions required to make a good IC AFM image. The cantilever's energy must be high enough such that it is not captured by the sample adhesion, that is, it must either be stiff or driven at high amplitudes. To remain to first order independent of the sample's properties, the setpoint amplitude should not be too low.

An IC AFM image is not independent of the mechanical properties of the sample, particularly for low setpoints and high-damping materials. In other words, true topographic imaging may be possible only under a limited set of conditions. To extract mechanical properties from IC AFM images will also prove to be challenging. Both the amplitude and phase of the cantilever response depend on $\bar{Q}_i^{-1}$ and λ for any given $\bar{Q}_c^{-1}$, $\bar{K}_c$ and $\bar{\Delta}$. Additional information beyond the IC AFM image is needed to separate their influence on the cantilever behaviour. For imaging and measurement of materials properties such as elastic stiffness the UFM-SLAM family of techniques will generally be more useful than the intermittent-contact mode.

4. Conclusions

IC AFM is proving extremely useful for a range of applications, especially with compliant samples. There is already a well established and growing community of users of IC AFM. For these users we hope that the simulations presented here will provide the basis of understanding for interpreting intermittent-contact images. Other techniques in which the cantilever vibrates are becoming increasingly accepted, especially for obtaining nanoscale information about the local elastic properties of stiffer materials. We hope that consideration of the model discussed here will help researchers to understand their results better, encourage new users to have confidence in the interpretation, and stimulate the development of different vibrating probe techniques for other needs and applications.

Acknowledgments

Without the help of the British Council/Swiss National Fund Joint Research Programme this cooperative paper would not have been possible. Partial support was provided by the European Community Human Capital and Mobility Programme project no CHRX-CT94-0668. The authors extend their thanks to Professor Jim Greenwood for his review of the manuscript. Finally, NAB wishes to express the warmest possible appreciation to her husband for his

support and for his acute insights during critical phases of the Fortran programming.

References

[1] Zhong Q, Inniss D, Kjoller K and Elings V B 1993 *Surf. Sci. Lett.* **290** L688–92

[2] Chernoff D A 1995 High resolution chemical mapping using tapping mode AFM with phase contrast *Proc. Microscopy and Microanalysis 1995*

[3] Umemura K, Arakawa H and Ikai A 1993 *Japan. J. Appl. Phys.* **32** L1711–14

[4] Bustamante C and Keller D 1995 *Phys. Today* December 32–8

[5] Howard A J, Rye R R and Houston J E 1996 *J. Appl. Phys.* **79** 1885–90

[6] Gregor M J, Blome P G, Schöfer J and Ulbrich R G 1996 *Appl. Phys. Lett.* **68** 307–9

[7] Giessibl F J 1995 *Science* **267** 68–71

[8] Chen G Y, Warmack R J, Huang A and Thundat T 1995 *J. Appl. Phys.* **78** 1465–9

[9] Anczykowski B, Krüger D and Fuchs H 1996 *Phys. Rev.* B **53** 15485–8

[10] Spatz J P, Sheiko S, Möller M, Winkler R G, Reineker P and Marti O 1995 *Nanotechnology* **6** 40–4

[11] Sarid D, Ruskell T G, Workman R K and Chen D 1996 *J. Vac. Sci. Technol.* B **14** 864–7

[12] Winkler R G, Spatz J P, Sheiko S, Möller M, Reineker R and Marti O 1996 *Phys. Rev.* B **54** 8908–12

[13] Tamayo J and García R 1996 *Langmuir* **12** 4430–5

[14] Sarid D, Chen J and Workman R K 1995 *Comput. Mat. Sci.* **3** 475–80

[15] Putman C A J, Van der Werf K O, De Grooth B G, Van Hulst N F and Greve J 1994 *Appl. Phys. Lett.* **64** 2454–6

[16] Chen J, Workman R K, Sarid D and Höper R 1994 *Nanotechnology* **5** 199–204

[17] Maugis D 1992 *J. Coll. Interface Sci.* **150** 243–69

[18] Maugis D and Gauthier-Manuel B 1994 *J. Adhesion Sci. Technol.* **8** 1311–22

[19] Muller V M, Yushenko V S and Derjaguin B V 1980 *J. Colloid Interface Sci.* **77** 91

[20] Johnson K L 1985 *Contact Mechanics* (Cambridge: Cambridge University Press)

[21] Derjaguin B V, Muller V M and Toporov Y P 1975 *J. Coll. Interface Sci.* **53** 314–26

[22] Sperling G 1964 Eine Theorie der Haftung von Feststoffteilchen an festern Körpern *PhD Thesis* Fakultät der Maschinenwesen T H Karlsruhe

[23] Johnson K L, Kendall K and Roberts A D 1971 *Proc. R. Soc.* A **324** 301–13

[24] Burnham N A and Colton R J 1993 Force microscopy *Scanning Tunneling Microscopy and Spectroscopy: Theory, Techniques and Applications* ed D A Bonnell (New York: VCH) pp 191–249

[25] Hughes B D and White L R 1979 *J. Mech. Appl. Math.* **32** 445

[26] Greenwood J A *Proc. R. Soc.* accepted

[27] Dugdale D S 1960 *J. Mech. Phys. Solids* **8** 100

[28] Burnham N A, Colton R J and Pollock H M 1993 *Nanotechnology* **4** 64–80

[29] Israelachvili J N 1985 *Intermolecular and Surface Forces* (New York: Academic)

[30] Burnham N A, Colton R J and Pollock H M 1992 *Phys. Rev. Lett.* **69** 144–7

[31] Chen G Y, Warmack R J, Oden P I and Thundat T 1996 *J. Vac. Sci. Technol.* B **14** 1313–7

[32] Kolosov O and Yamanaka K 1993 *Japan. J. Appl. Phys.* **32** L1095–8

[33] Yamanaka K 1995 New approaches in acoustic microscopy for noncontact measurement and ultrahigh resolution *Advances in Acoustic Microscopy* vol I, ed G A D Briggs (New York: Plenum)

[34] Burnham N A, Kulik A J, Gremaud G, Gallo P-J and Oulevey F 1996 *J. Vac. Sci. Technol.* B **14** 794–9

[35] Burnham N A, Kulik A J, Gremaud G and Briggs G A D 1995 *Phys. Rev. Lett.* **74** 5092–5